IEEE Access
Multidisciplinary | Rapid Review | Open Access Journal

Received December 17, 2020, accepted February 13, 2021, date of publication February 16, 2021, date of current version March 1, 2021.

Digital Object Identifier 10.1109/ACCESS.2021.3059797

Research on the Parameter Design Method and System Simulation of Multimode Microwave Remote Sensors Operating in Scatterometer Modes

PENG ZHOU[1], (Member, IEEE), LIAN XUE[1], ZHENHUA ZHANG[2], YING WANG[2], AND XI ZHANG[3]

[1]College of Oceanography and Space Informatics, China University of Petroleum, Qingdao 266580, China
[2]Beijing Research Institute of Telemetry, Beijing 100076, China
[3]First Institute of Oceanography, Ministry of Natural Resources of the People's Republic of China, Qingdao 266061, China

Corresponding author: Peng Zhou (zhoupeng@upc.edu.cn)

This work was supported in part by the National Key R&D Program of China under Grant 2017YFC1405600, in part by the Shandong Provincial Natural Science Foundation under Project ZR2019MF004, in part by the Youth Fund of China Marine Telemetry Engineering Research Center under Grant 2017003, and in part by the Project Sponsored by the First Institute of Oceanography in Ministry of Natural Resources under Grant N1705037.

ABSTRACT Multimode microwave remote sensors are a new type of radar system that operates in SAR (synthetic aperture radar), scatterometer, altimeter, and spectrometer modes in a time-sharing manner according to the current task scheduled on small satellites. High flexibility through mode switching is the outstanding advantage of this new microwave remote sensor. Two or more small satellites operating in different operation modes can be networked to perform observations synchronously to provide excellent remote sensing performance. This paper focuses on a method to determine the radar parameters of the scatterometer mode since the frequency band and the platform height of this new of kind sensor are determined according to the requirement of the SAR mode, and their values are evidently different from the values of current scatterometers in orbit. The proposed method systematically presents the complete steps and related formulae of the radar parameter design of scatterometers and determines the signal bandwidth by optimization. A system simulation method of the scatterometer mode is further studied to determine the wind field inversion error and thus evaluate the rationality of the parameter design results. In contrast to the existing methods, which directly add noise to the backscatter coefficients, our method simulates the noisy echo of the scatterometer and then retrieves the wind field by estimated backscatter coefficients from the noisy echo. The performed simulation shows that, by using the designed system parameters, the multimode microwave remote sensor obtains wind field inversion accuracy, resolution and swath width comparable to those of the HY-2 satellite and the QuikSCAT satellite.

INDEX TERMS Multimode microwave remote sensor, scatterometer mode, system parameter design method, system simulation, inversion accuracy of wind field.

I. INTRODUCTION

Multimode microwave remote sensors are a new type of radar system mounted on small satellite platforms [1], [2]. Here, small satellites refer to satellites whose weights are between 100 and 500 kg. It takes advantage of the flexible beam control ability contributed by two-dimensional phased array antennas [3]. Multiple SAR (synthetic aperture radar) imaging modes, such as strip maps, spotlights and scanning, as well as dynamic marine parameter detection modes, such as altimeter [4], scatterometer [5]–[11] and spectrometer modes [12], can be realized in a time-sharing manner. Multimode microwave remote sensors have high flexibility and can realize both high-precision target detection and high-precision inversion of dynamic marine parameters. More specifically, a suitable mode can be selected according

The associate editor coordinating the review of this manuscript and approving it for publication was Junjie Wu.

to the current scheduled task of the small satellite. SAR mode is good at land observation and sea target detection. Altimeter mode can provide information such as sea surface height, significant wave height and wind speed. The inversion accuracy of the wind speed and the wind direction is high with regards to the scatterometer mode. The spectrometer mode can provide the information of the wave spectrum. Furthermore, two or more multimode microwave remote sensors can be networked to improve the detection capability. For example, two small satellites working in the SAR mode and the scatterometer mode, respectively, can simultaneously observe a certain sea area and improve the accuracy of wind field inversion through joint inversion [13]. Another example is that two networked small satellites operating in the scatterometer and spectrometer modes, respectively, can carry out high-precision joint inversion of wind and wave simultaneously [14]. Thus, the multimode microwave remote sensor under development has good development prospects. This paper concentrates on the parameter design method and the system simulation of the multimode microwave remote sensor operating in the scatterometer mode. Similar to spaceborne scatterometers, one of the main tasks of the scatterometer mode for the multimode microwave remote sensor is to perform wind inversion of global ocean surfaces. Moreover, the wind field of the ocean surface can also be retrieved from SAR images and altimeter data. The main advantage of SAR systems for wind retrieval is their high resolution, whereas their disadvantage is their relatively small swath width, which is generally less than 100 km. Altimeters can provide wind products at the kilometer resolution scale along the satellite track, but their disadvantage is that their swath width is narrow and can provide only wind speed. Scatterometers are currently the main instrument for wind field observation of the global ocean surface due to their swath width that exceeds 1000 km and their multi-aspect measurement ability, which can be used to invert the wind direction.

The SAR mode is the main mode of this new radar system. Some important parameters, such as the carrier frequency and the platform height of other modes, must be consistent with those of the SAR mode. The SAR mode has been designed to operate in the X-band with a platform height of 530 km. At present, spaceborne scatterometers generally work in the C or Ku band [15]–[18], and the height of the associated satellites is generally 700-1000 km [15]–[18]. Therefore, the existing scatterometer system parameters cannot be applied to multimode microwave remote sensors. This implies that a method for specifying the system parameters for the scatterometer mode of multimode microwave remote sensors must be developed. Furthermore, the development of a software simulation system is needed to estimate the inversion accuracy of wind speed and wind direction to verify the feasibility of applying multimode microwave remote sensors for wind field inversion of global sea surfaces.

Many related studies have been carried out on the parameter design and software simulation system construction of spaceborne scatterometers. Reference [19] introduces the performance indicators of NSCAT (NASA Scatterometer Satellite), the design of antenna subsystems and resolution, and the accuracy analysis of wind field inversion. In reference [20], the influence of signal fading and thermal noise is separated, and factors such as attenuation in signal propagation are considered. It establishes the measurement model of scatterometers and simulates random changes in scatterometer measurements to evaluate the system performance. References [21] and [22] introduce the performance indicators, system parameters and wind field inversion accuracy analysis of a Ku-band fan-beam rotating scanning scatterometer. Generally, the existing literature mainly presents the system parameter design results of scatterometers, and therefore, it lacks a complete discussion of the system parameter design method for scatterometers. In other words, a method comprising complete and detailed steps and relevant formulae of each step to determine radar parameters of scatterometers is required.

In this paper, the design method for the system parameters of multimode microwave remote sensor systems working in the scatterometer mode is studied. First, the advantages and disadvantages of three mechanisms, including a fixed fan-beam, rotating pencil-beam and rotating fan-beam, are compared, and the rotating pencil-beam mechanism is selected to be used in the multimode microwave remote sensor operating in scatterometer modes. By analyzing the constraint relationship between the system performance indicators and the system operating parameters, the complete design steps of the system operating parameters are summarized, and the relevant formulas for determining the system operating parameters are derived. The determination of the signal bandwidth is performed by optimization to minimize the relative error sum of the wind speed and the wind direction. To verify the rationality of the parameter design results, a software simulation system is developed. The system simulation model, the sea surface simulation method, the geophysical model function, the backscatter coefficient measurement method and the wind field inversion algorithm in our research are introduced. The existing methods of simulating scatterometers usually add noise directly to the backscatter coefficient of the sea surface. By contrast, our method generates the noisy echo of scatterometers and then retrieves the wind field through estimated backscatter coefficients. Thus, our method is closer to the real processing procedure of actual scatterometers. Simulation experiments were carried out, and the simulation results verified the rationality of the designed system parameters.

II. SYSTEM PARAMETER DESIGN FOR MULTIMODE MICROWAVE REMOTE SENSORS OPERATING IN SCATTEROMETER MODES

A. THE CHOICE OF WORKING MECHANISM

There are three common working mechanisms for spaceborne scatterometers: the fixed fan-beam mechanism [19], rotating pencil-beam mechanism [23] and rotating fan-beam

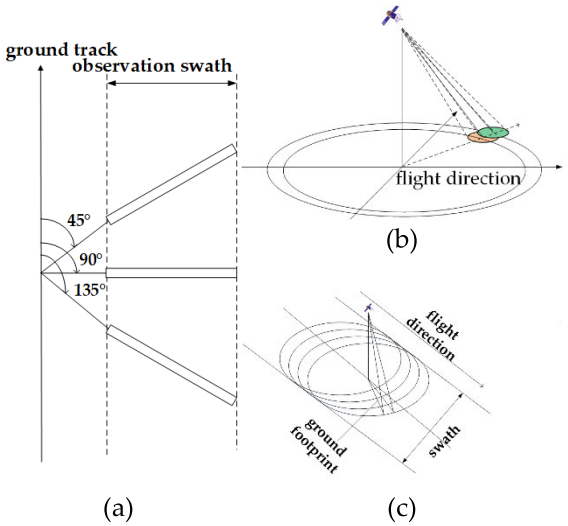

FIGURE 1. Observation geometry of scatterometers under three different mechanisms: (a) Fixed fan-beam mechanism; (b) Rotating pencil-beam mechanism; (c) Rotating fan-beam mechanism.

TABLE 1. Comparison of three common mechanisms of spaceborne scatterometers.

	fixed fan-beam	rotating pencil-beam	rotating fan-beam
antenna	multiple antennas	larger than that of rotating fan-beam	smaller than that of rotating pencil-beam
scan speed	no scanning	fast	slow
signal-to-noise ratio	low	high	low
number of independent samples	large	small	large
swath	narrow	wide	wide
swath continuity	discontinuous near subsatellite point	continuous	continuous
data processing complexity	complicated	easy	complicated

mechanism [24]. Fig.1 shows the observation geometries under the three mechanisms. Table 1 provides a comprehensive comparison of the three mechanisms in terms of antenna characteristics, scanning speed, signal-to-noise ratio, number of independent samples, swath width, continuity of detection areas and data processing complexity.

Table 1 compares the fixed fan-beam mechanism, the rotating pencil-beam mechanism, and the rotating fan-beam mechanism from several aspects. With regard to the fixed fan-beam mechanism, the area near the subsatellite point is a blind spot in terms of data acquisition, so the coverage rate of this kind of system is the lowest among the three mechanisms. Hence, this mechanism is rarely used in modern scatterometer systems. Compared with the rotating pencil-beam mechanism, the rotating fan-beam mechanism features a smaller antenna size and a lighter weight since its beamwidth is larger. Therefore, the traditional view is that the rotating fan-beam mechanism is more suitable for small satellite platforms. However, with the development of antenna technology, two-dimensional lightweight phased array antennas have gradually come to be used in microwave remote sensors such as scatterometers. Because bulky antenna servo equipment is not required when phased array antennas are employed, it is possible to apply a rotating pencil-beam mechanism on small satellite platforms. Further, the data processing under the rotating pencil-beam mechanism is easier than that under the rotating fan-beam mechanism because the beam is narrow both in the azimuth direction and in the range direction under the rotating pencil-beam mechanism. More specifically, the characteristic that the incidence angles are the same for different range cells simplifies the data processing under the rotating pencil-beam mechanism. In addition, the antenna gain of the rotating pencil-beam mechanism is high, so it can obtain a high signal-to-noise ratio, which is beneficial to inversions under low wind speeds. Based on the above considerations, in this paper, the rotating pencil-beam mechanism is selected for use in multimode microwave remote sensor systems operating in scatterometer mode.

B. SYSTEM PARAMETER DESIGN METHOD BASED ON THE CONSTRAINT RELATIONSHIP BETWEEN SYSTEM PARAMETERS AND PERFORMANCE INDICATORS

When designing the system parameters of multimode microwave remote sensors operating in scatterometer mode, the performance indicators generally required to be specified by users include the ground range resolution ρ_{gr}, azimuth resolution ρ_{az}, internal beam swath W_n, external beam swath W_f, and normalized standard deviation of echo power K_p. The parameters that should be consistent with the SAR mode include the platform height H, the platform speed v, the platform ground speed v_g and the carrier frequency f_c. The radar parameters to be given or selected by combining various factors include the number of beams M, the tangential velocity of the beam footprint scanning on the ground v_t, the pulse width T_r, the receiver noise figure F, the system loss L_s, and the normalized equivalent noise figure $NE\sigma^0$. The radar parameters to be outputted as the design results include the view angles and the incidence angles of the inner and outer beams, the slant ranges corresponding to the inner beam and the outer beam, the range beam width, the azimuth beam width, the range antenna size, the azimuth antenna size, the antenna rotation speed, the pulse repetition frequency, the signal bandwidth, the bandwidth after the dechirp processing, the signal-to-noise ratio and the transmitted peak power.

In the first step, the view angles and the incidence angles of the inner and outer beams are determined according to the requirements of the swaths of the inner and outer beams. According to the geometric relationship, the relationship between the view angle α and the incidence angle θ is as follows:

$$\sin\theta = \frac{R_e + H}{R_e}\sin\alpha \tag{1}$$

where R_e is the average radius of the earth. The relationships between the swaths, the view angles and the incident angles of the inner beam and the outer beam are as follows:

$$W_n = 2 \cdot R_e \cdot (\theta_n - \alpha_n) \tag{2}$$

$$W_f = 2 \cdot R_e \cdot (\theta_f - \alpha_f) \tag{3}$$

where α_n and θ_n are the view angle and the incident angle of the inner beam, respectively, and α_f and θ_f are the view angle and the incident angle of the outer beam, respectively. Obviously, according to formulas numbered (1), (2) and (3), the view angles and the incidence angles of the inner and outer beams can be determined according to the requirements of the internal and external beam swaths.

In the second step, R_n and R_f, the slant ranges corresponding to the inner beam and the outer beam are first calculated. Then, the range beam width φ_r and the azimuth beam width φ_a are computed. Afterwards, the range antenna size l_r and the azimuth antenna size l_a are finally determined. The corresponding formulas are as follows:

$$R_n = \frac{\sin(\theta_n - \alpha_n)}{\sin \alpha_n} \cdot R_e \tag{4}$$

$$R_f = \frac{\sin(\theta_f - \alpha_f)}{\sin \alpha_f} \cdot R_e \tag{5}$$

$$\varphi_r = \frac{\rho_{gr} \cdot \cos \theta_f}{R_f} \tag{6}$$

$$\varphi_a = \frac{\rho_{az}}{R_f} \tag{7}$$

$$l_r = \frac{\lambda}{\varphi_r} \tag{8}$$

$$l_a = \frac{\lambda}{\varphi_a} \tag{9}$$

where λ is the radar wavelength.

In the third step, the lower limit of the antenna rotation speed Ω, and the upper and lower limits of the pulse repetition frequency PRF are determined. According to the requirement of continuous coverage along the trajectory of subsatellite points, the following results can be obtained:

$$\Omega \geq 2\pi \cdot \frac{v_g}{\rho_{gr}} \tag{10}$$

According to the requirement of continuous coverage along the scanning direction, the following results can be obtained:

$$PRF \geq M \cdot \frac{v_t}{\rho_{az}} \tag{11}$$

According to the requirement of avoiding range ambiguity, the following results can be obtained:

$$PRF \leq \frac{C}{2\rho_{gr} \sin \theta_f} \tag{12}$$

where C is the speed of light. When selecting the specific value between the upper and lower limits of PRF, the return time of the echo should avoid the period of the pulse transmission and the return time of the subsatellite point echo [25].

Step 4 is to determine the signal bandwidth using the optimization approach. By comparing the root mean square (RMS) errors of wind speed and wind direction inversions under different wind speed and bandwidth conditions, the optimal bandwidth is selected. The signal bandwidth B is determined by the following optimization criteria:

$$B = \arg\min_{B} \left[rdv_{rms}(B) + rd\varphi_{rms}(B) \right] \tag{13}$$

where rdv_{rms} and $rd\varphi_{rms}$ are the RMS errors of the wind speed relative error and wind direction relative error, respectively [26].

In the fifth step, the bandwidth after the dechirp processing B_s is determined. According to the geometric relationship, it is given by:

$$B_s = \frac{2\rho_{gr} \cos \theta_f}{CT_r} \cdot B \tag{14}$$

Step 6 is to determine the value of the signal-to-noise ratio SNR. According to the relationship between the normalized standard deviation of echo power K_p and the signal-to-noise ratio SNR, the required SNR values can be calculated by [19]:

$$K_p = \sqrt{\frac{\left(1 + \frac{1}{SNR}\right)^2 + \left(\frac{1}{SNR}\right)^2}{N}} \tag{15}$$

where N is the number of independent samples, and there are:

$$N = 4B_sT_r \tag{16}$$

After the required SNR is calculated according to equation (15), for the sake of safety, it is generally considered best to take twice the calculated value as the output value.

Finally, the peak power P_t is calculated according to the radar equation:

$$P_t = \frac{(4\pi)^3 \cdot R_f^4 \cdot L_s \cdot k_b B T_0 F \cdot SNR}{G^2 \cdot \lambda^2 \cdot NE\sigma^0 \cdot \rho_{gr} \cdot \rho_{az} \cdot \sqrt{B_sT_r}} \tag{17}$$

where k_b is the Boltzmann constant, $T_0 = 290$ K, and G is the antenna gain.

Fig. 2 summarizes the parameter design process of our proposed method for a multimode microwave remote sensor operating in scatterometer modes.

III. SYSTEM SIMULATION OF MULTIMODE MICROWAVE REMOTE SENSORS OPERATING IN SCATTEROMETER MODES

The system simulation of the scatterometer mode is carried out to verify the rationality of the parameter design results after the design process of the system. The wind field inversion error is evaluated by comparing the set wind field with the inverted wind field to measure the rationality of the parameter design results. Fig. 3 shows the flow chart of the system simulation for the scatterometer mode.

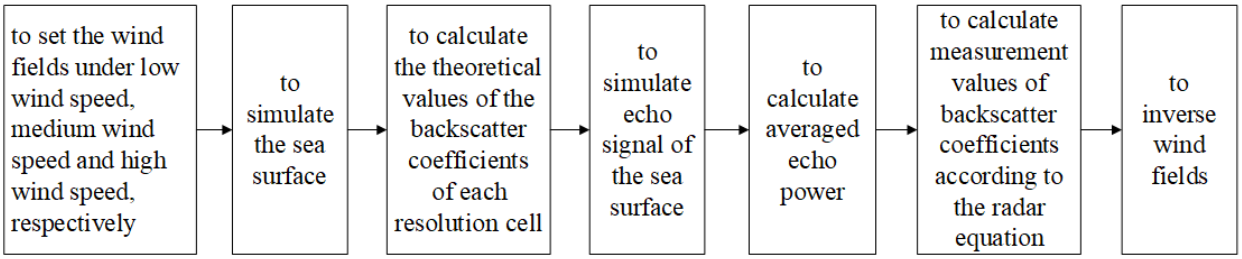

FIGURE 3. Flow chart of system simulation for scatterometer modes.

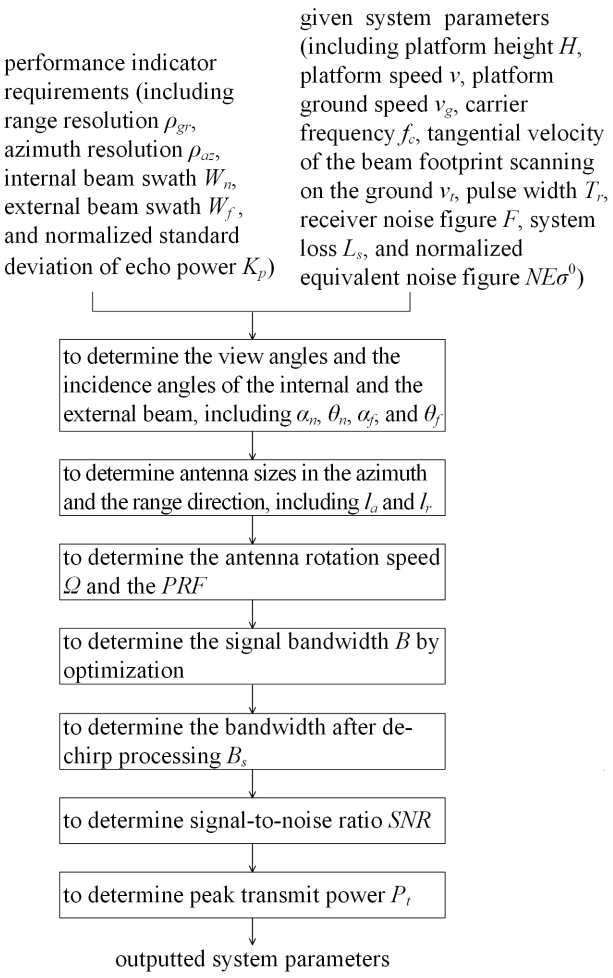

FIGURE 2. Flowchart of the proposed parameter design method based on constraints between system parameters and performance indicators.

A. SEA SURFACE SIMULATION

At present, the sea surface simulation method involves generating the wave spectrum first and then simulating the sea surface according to the generated wave spectrum. Common wave spectrum models include the PM spectrum, JONSWAP spectrum, and DV spectrum. In this paper, the PM spectrum, which is simple and widely used, is selected to simulate the sea surface. The PM spectrum is the wave spectrum obtained by Pierson and Moscowitz after spectrum estimation and curve fitting of the wind wave data in the fully growing state of the Atlantic Ocean. It is easy to simulate and close to the actual wave spectrum.

The wavenumber spectrum model of the main wave direction of the PM spectrum is as follows [27]:

$$S_{PM}(k) = \frac{a}{2k^4}\exp\left(-\frac{bg^2}{k^2U^4}\right) \tag{18}$$

where $a = 0.0081$, $b = 0.74$, k is the spatial wavenumber of the sea waves, U is the wind speed at 19.5 m above the sea surface, and g is the acceleration due to gravity.

The two-dimensional PM spectrum can be expressed as follows [27]:

$$S_{PM}(k, \varphi_v) = \frac{a}{2k^4}\exp\left(-\frac{bg^2}{k^2U^4}\right)\cos^4(\varphi_v - \varphi) \tag{19}$$

where φ_v is the direction of the observation and φ is the wind direction.

After obtaining the wave spectrum, the two-dimensional sea surface can be simulated. In this paper, the linear filtering method is used to simulate the sea surface. The height $h(x_m, y_n)$ at each cell on the rough sea surface can be expressed as [27], (20) as shown at the bottom of the next page, where (x_m, y_n) are the x and y coordinates of the cell's center position, respectively; L_x and L_y represent the length of the simulated two-dimensional sea surface in azimuth and range, respectively; M' and N' are the number of sampling points in azimuth and range, respectively; $S(k_m, k_n)$ is the two-dimensional wave spectrum of the simulated rough sea surface in Cartesian coordinates; and $N(0, 1)$ is a random number satisfied with the Gaussian distribution with a zero mean value and a standard deviation of 1.

Fig. 4 shows the simulation results of the two-dimensional sea surface under four different wind speed and wind direction settings. The wind speeds and the wind directions corresponding to subfigures (a), (b), (c) and (d) in Fig.4 are 15 m/s and 0°, 10 m/s and 0°, 10 m/s and 45°, and 5 m/s and 90°, respectively. The wind direction here refers to the angle that deviates anticlockwise from the radar line of sight. Fig. 4 shows that the sea height changes obviously with changes in the wind speed and the wind direction. The higher the wind speed, the more fluctuation is observed in the sea surface's height. When the wind direction is consistent with

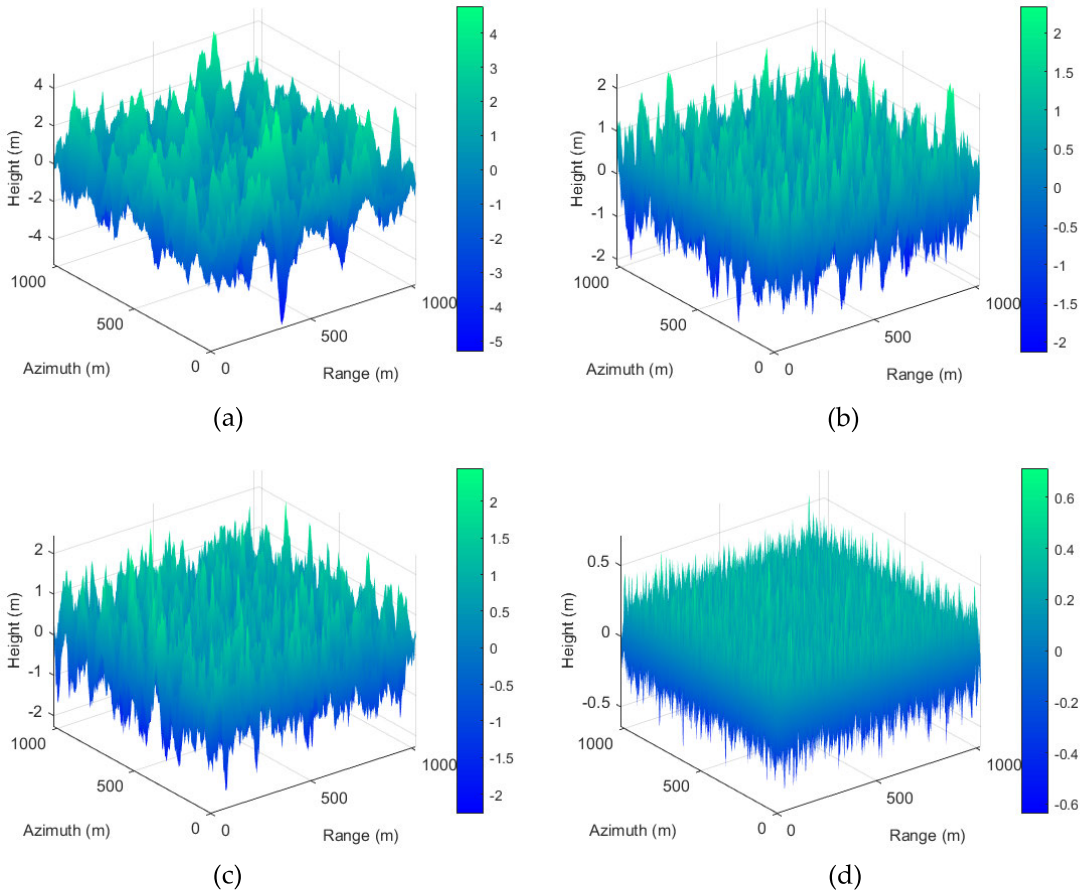

FIGURE 4. Two-dimensional sea surface simulation results under different wind speed and wind direction settings: (a) Wind speed 15 m/s, wind direction 0°; (b) Wind speed 10 m/s, wind direction 0°; (c) Wind speed 10 m/s, wind direction 45°; (d) Wind speed 5 m/s, wind direction 90°.

the radar line of sight, the sea surface's height fluctuates greatly.

B. XMOD2 GEOPHYSICAL MODEL FUNCTION

The relationship between the radar backscattering coefficient and wind direction, wind speed, radar incidence angle, polarization mode, carrier frequency, sea surface temperature and other influencing factors is gradually established in the research of sea surface wind field inversion using scatterometer observation data. This functional relationship is called the geophysical model function (GMF) [28]. The general form of GMF can be expressed as follows:

$$\sigma_m^0 = M\left(U, \varphi - \varphi_v, \theta, p, f_c, L\right) \tag{21}$$

where σ_m^0 is the normalized backscattering coefficient of the sea surface calculated by the model, U is the wind speed above the sea surface, φ is the wind direction angle, φ_v is the azimuth angle of the radar line of sight, θ is the incidence angle, p is the polarization mode, f_c is the carrier frequency, and L represents other auxiliary factors.

The XMOD2 GMF is the latest model used for X-band observation data, and its function form is [29]:

$$\sigma_m^0 = B_0\left\{1 + B_1\cos\left(\varphi - \varphi_v\right) + B_2\cos\left[2\left(\varphi - \varphi_v\right)\right]\right\} \tag{22}$$

where B_0, B_1 and B_2 are functions related to the wind speed above the sea surface and the incidence angle. Fig. 5 shows the relationship between the normalized backscatter coefficient of the sea surface and the wind speed based

$$h\left(x_m, y_n\right) = \frac{1}{L_x L_y}\sum_{m=-M'/2+1}^{M'/2}\sum_{n=-N'/2+1}^{N'/2} H\left(k_m, k_n\right)\exp\left[j\left(k_m x_m + k_n y_n\right)\right]$$
$$H\left(k_m, k_n\right) = 2\pi\sqrt{L_x L_y S\left(k_m, k_n\right)}\times\begin{cases}\sqrt{2}\left[N\left(0,1\right) + j\cdot N\left(0,1\right)\right], m\neq 0, m\neq M'/2, n\neq 0, n\neq N'/2\\ N\left(0,1\right), m = 0 \text{ or } m = M'/2 \text{ or } n = 0 \text{ or } n = N'/2\end{cases} \tag{20}$$

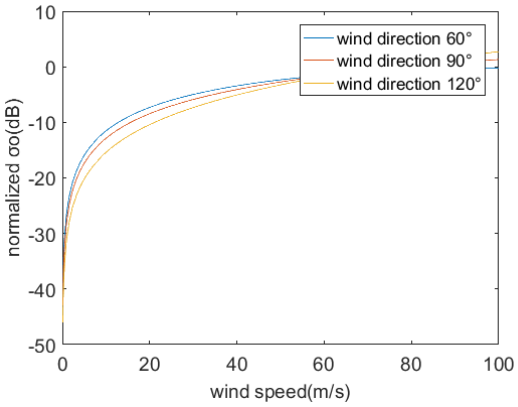

FIGURE 5. Changes in the normalized radar cross section with wind speed.

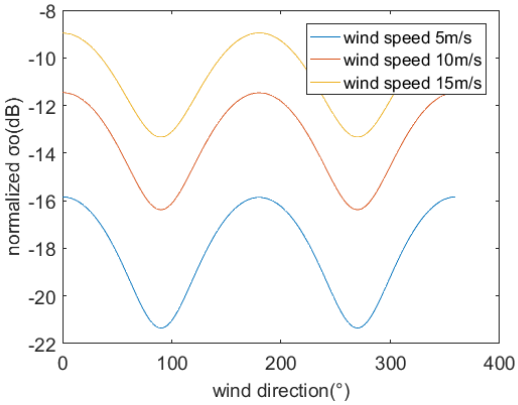

FIGURE 6. Changes in the normalized radar cross section with wind direction.

on the XMOD2 model. Fig. 6 depicts the relationship between the normalized backscatter coefficient of the sea surface and the wind direction. The wind direction here also refers to the angle that deviates anticlockwise from the radar line of sight. It can be seen from these two figures that the backscattering coefficient of the sea surface increases with increasing wind speed and changes in a cosine-like function with the wind direction. The backscattering coefficient is the highest downwind and the lowest crosswind.

C. TO OBTAIN THE MEASURED VALUES OF BACKSCATTERING COEFFICIENTS

The transmitter of the scatterometer generates a linear frequency modulation (LFM) signal and transmits the signal to the sea surface through its antenna. The incident wave arrives at the sea surface and scatters back to the radar. After being received by the antenna and the receiver, the measured values of the backscattering coefficients of the sea surface can be obtained by the signal processor.

The LFM signal transmitted by a radar can be expressed as follows:

$$S_t(t) = \text{rect}\left(\frac{t}{T_r}\right)\exp\left[j\left(2\pi f_c t + \pi k_r t^2\right)\right] \tag{23}$$

where k_r is the slope of the LFM and rect represents a rectangular function. The echo signal modulated by the sea surface can be expressed as (24), shown at the bottom of the page, where σ_i^0, A_i and G_i are the normalized radar cross section, the cover area and the antenna gain corresponding to the i-th range bin respectively, and R_i is the distance between the i-th range bin and the radar.

The reference target's distance is denoted as R_{ref}, and the echo signal after dechirp processing can be expressed as follows [30], (25) as shown at the bottom of the page.

To simulate the influence of the receiver noise, it is necessary to generate a receiver noise signal. The noise power of the receiver input is as follows:

$$N_i = k_b T_0 B \tag{26}$$

After calculating the noise power at the receiver input using equation (26), complex Gaussian noise with a zero mean value and a variance of N_i is generated and superimposed on the echo signal at the receiver input. After dechirp processing is performed on the echo signal at the input of the receiver, the echo signal at the output of the receiver is obtained.

The calculation formula of the echo power at the output of the receiver is as follows:

$$P_r = \frac{1}{N_{valid}}\sum_{k=1}^{N_{valid}} |f(k)|^2 \tag{27}$$

where $f(k)$ is the echo signal of the receiver output after discretization and N_{valid} is the number of valid sampling points.

After obtaining the echo power of the receiver output, the normalized backscatter coefficient σ_{ri}^0 of the corresponding resolution cell of the sea surface can be calculated from the radar equation [31]:

$$\sigma_{ri}^0 = \frac{P_r(4\pi)^3 R^4 L_s}{P_t \lambda^2 A G^2} \tag{28}$$

$$S_r(t) = \sum_i \left\{ \sqrt{\frac{P_t \cdot \lambda^2 \cdot \sigma_i^0 \cdot A_i \cdot G_i^2}{(4\pi)^3 \cdot R_i^4 \cdot L_s}}\,\text{rect}\left(\frac{t-\frac{2R_i}{C}}{T_r}\right)\exp\left\{j\cdot\left[2\pi f_c\left(t-\frac{2R_i}{C}\right)+\pi k_r\left(t-\frac{2R_i}{C}\right)^2\right]\right\}\right\} \tag{24}$$

$$S_r'(t) = \sum_i \left\{ \begin{array}{l} \sqrt{\frac{P_t\cdot\lambda^2\cdot\sigma_i^0\cdot A_i\cdot G_i^2}{(4\pi)^3\cdot R^4\cdot L_s}}\,\text{rect}\left(\frac{t-\frac{2R}{C}}{T_r}\right)\text{rect}\left(\frac{t-\frac{2R_{ref}}{C}}{T_r}\right)\cdot \\ \exp\left\{j\cdot\left[-2\pi k_r\left(\frac{2R}{C}-\frac{2R_{ref}}{C}\right)t-2\pi f_c\left(\frac{2R}{C}-\frac{2R_{ref}}{C}\right)+4\pi k_r\frac{R^2-R_{ref}^2}{C^2}\right]\right\} \end{array} \right\} \tag{25}$$

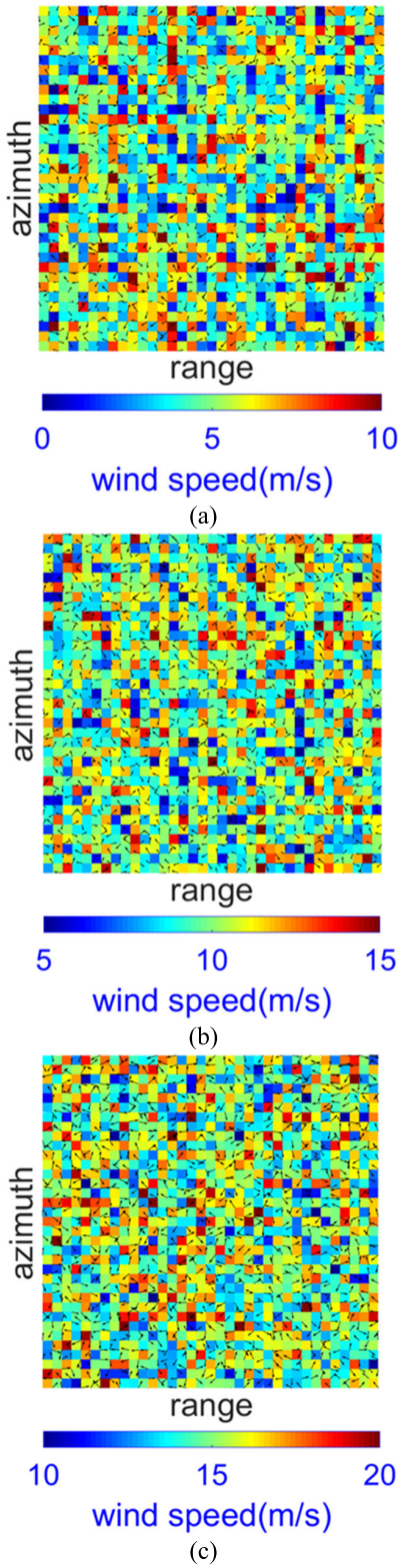

FIGURE 7. Distribution of one of the inputted random wind fields: (a) Low wind speed with a mean value of 5 m/s and a standard deviation of 2 m/s; (b) Medium wind speed with a mean value of 10 m/s and a standard deviation of 2 m/s; (c) High wind speed with a mean value of 15 m/s and a standard deviation of 2 m/s.

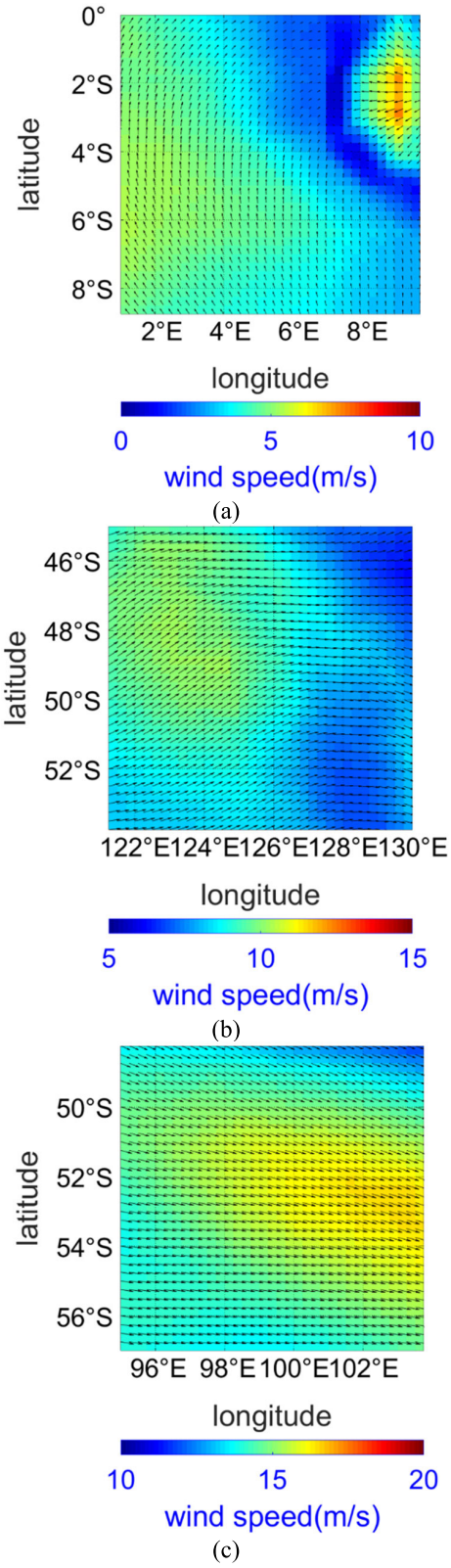

FIGURE 8. Distribution of inputted real wind fields: (a) Low wind speed; (b) Medium wind speed; (c) High wind speed.

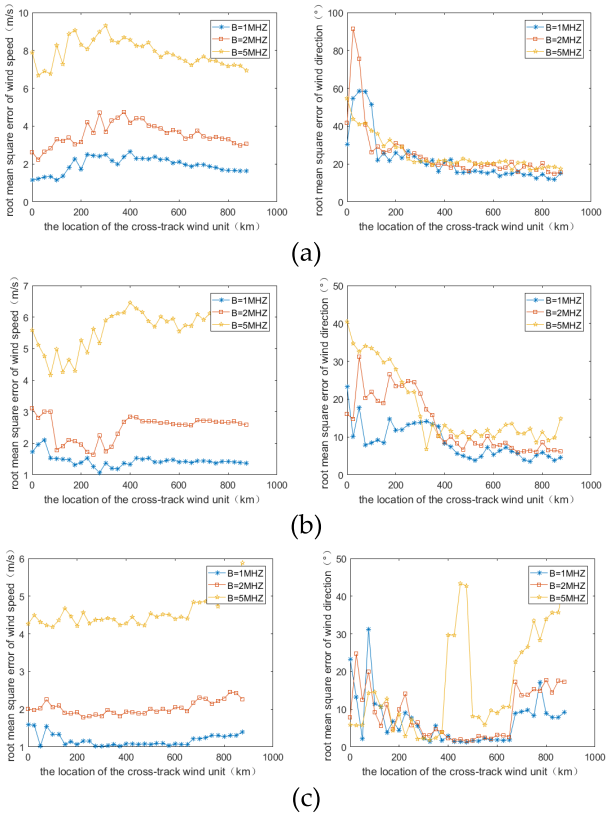

FIGURE 9. RMS errors of inverted wind speed and wind direction under different wind speed and bandwidth conditions for the selected real wind fields: (a) Low wind speed; (b) Medium wind speed; (c) High wind speed.

D. WIND FIELD INVERSION ALGORITHM OF SCATTEROMETERS

There are many kinds of wind field inversion algorithms for scatterometers, including the maximum likelihood estimation (MLE) method, weighted minimum variance method in the logarithmic domain, minimum wind speed variance method, etc. At present, the MLE method is mainly used in operational scatterometer systems. The objective function of MLE is as follows [32],[33]:

$$J_{MLE}(U,\varphi) = -\sum_{i=1}^{4}\left[\sigma_{ri}^{0} - \sigma_{mi}^{0}(U,\varphi-\varphi_{vi})\right]^{2} \quad (29)$$

where σ_{ri}^{0} is the i-th measured value of the normalized backscatter coefficient of the current cell, φ_{vi} is the radar line of sight in azimuth corresponding to the i-th measured value, and σ_{mi}^{0} is the i-th model value of the normalized backscattering coefficient of the current cell.

When using scatterometer data to retrieve the sea surface wind field, due to the harmonic characteristic of the GMF, some fuzzy wind field solutions are always obtained. At present, operational scatterometer systems often adopt the circle median filtering algorithm to filter out the fuzzy wind field solution and to obtain the final wind vector solution [34].

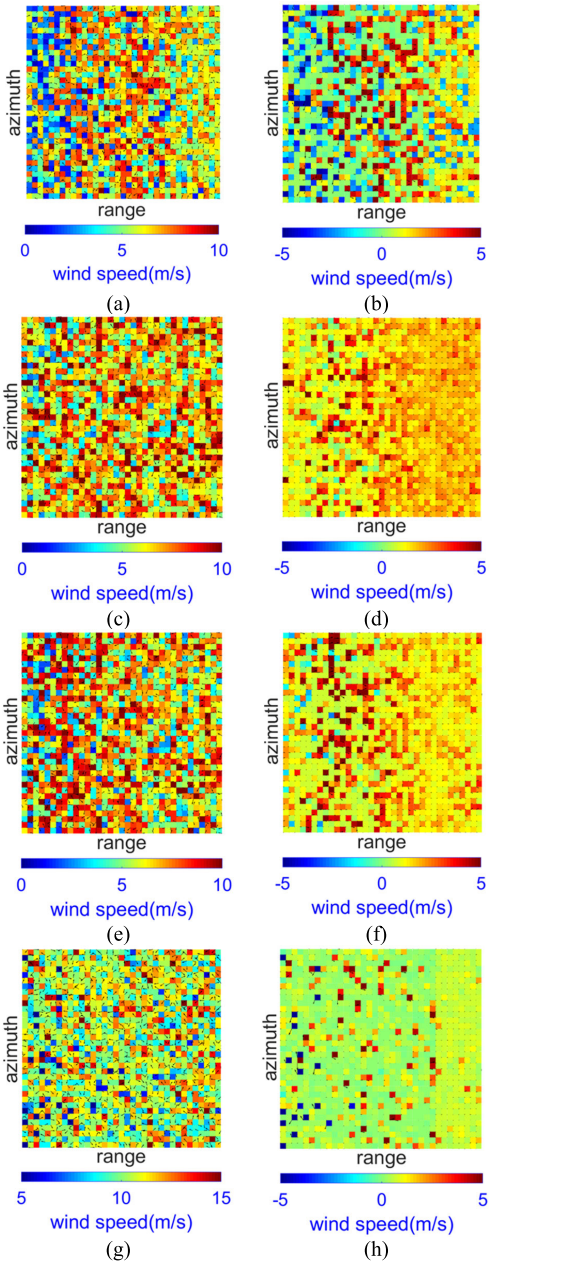

FIGURE 10. Inversion results and corresponding errors for the inputted random wind fields: (a) Inversion result of the designed X-band multimode microwave remote sensor with low wind speed; (b) Inversion errors of the designed X-band multimode microwave remote sensor with low wind speed; (c) Inversion result of the HY-2 satellite with low wind speed; (d) Inversion error of the HY-2 satellite with low wind speed; (e) Inversion result of the QuikSCAT satellite with low wind speed; (f) Inversion error of the QuikSCAT satellite with low wind speed; (g) Inversion result of the designed X-band multimode microwave remote sensor with medium wind speed; (h) Inversion errors of the designed X-band multimode microwave remote sensor with medium wind speed; (i) Inversion result of the HY-2 satellite with medium wind speed; (j) Inversion error of the HY-2 satellite with medium wind speed; (k) Inversion result of the QuikSCAT satellite with medium wind speed; (l) Inversion error of the QuikSCAT satellite with medium wind speed; (m) Inversion result of the designed X-band multimode microwave remote sensor with high wind speed; (n) Inversion errors of the designed X-band multimode microwave remote sensor with high wind speed; (o) Inversion result of the HY-2 satellite with high wind speed; (p) Inversion error of the HY-2 satellite with high wind speed; (q) Inversion result of the QuikSCAT satellite with high wind speed; (r) Inversion error of the QuikSCAT satellite with high wind speed.

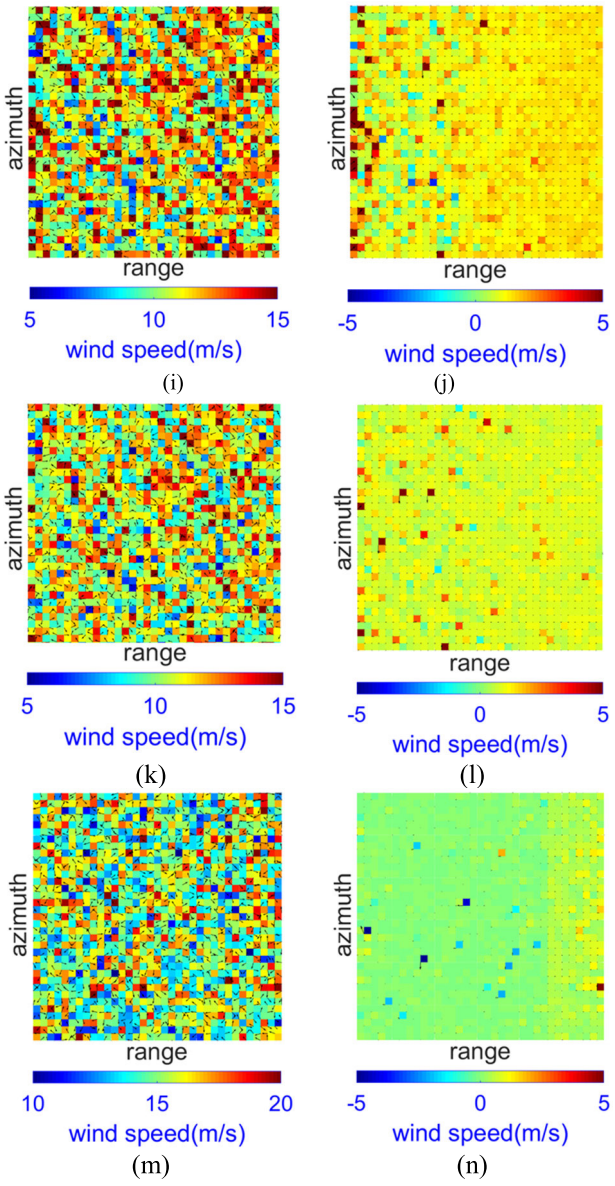

FIGURE 10. *(Continued.)* **Inversion results and corresponding errors for the inputted random wind fields: (a) Inversion result of the designed X-band multimode microwave remote sensor with low wind speed; (b) Inversion errors of the designed X-band multimode microwave remote sensor with low wind speed; (c) Inversion result of the HY-2 satellite with low wind speed; (d) Inversion error of the HY-2 satellite with low wind speed; (e) Inversion result of the QuikSCAT satellite with low wind speed; (f) Inversion error of the QuikSCAT satellite with low wind speed; (g) Inversion result of the designed X-band multimode microwave remote sensor with medium wind speed; (h) Inversion errors of the designed X-band multimode microwave remote sensor with medium wind speed; (i) Inversion result of the HY-2 satellite with medium wind speed; (j) Inversion error of the HY-2 satellite with medium wind speed; (k) Inversion result of the QuikSCAT satellite with medium wind speed; (l) Inversion error of the QuikSCAT satellite with medium wind speed; (m) Inversion result of the designed X-band multimode microwave remote sensor with high wind speed; (n) Inversion errors of the designed X-band multimode microwave remote sensor with high wind speed; (o) Inversion result of the HY-2 satellite with high wind speed; (p) Inversion error of the HY-2 satellite with high wind speed; (q) Inversion result of the QuikSCAT satellite with high wind speed; (r) Inversion error of the QuikSCAT satellite with high wind speed.**

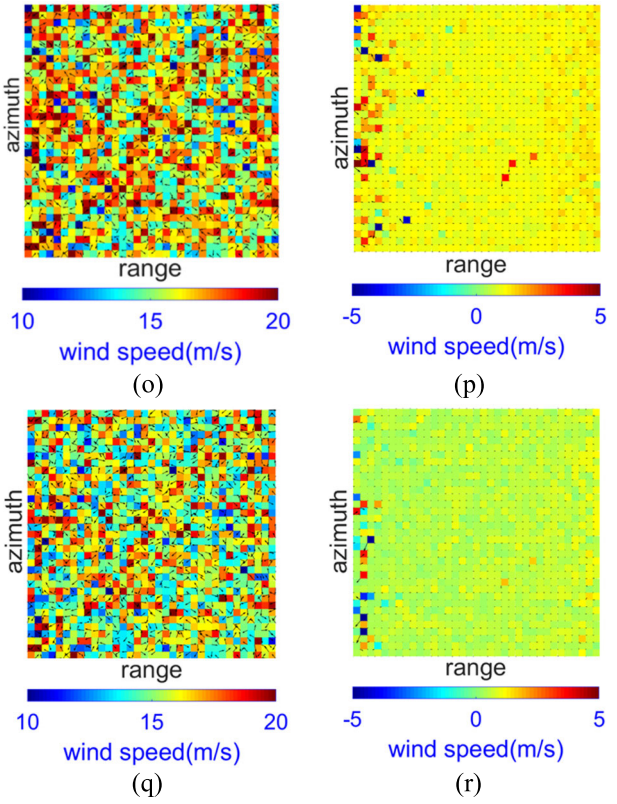

FIGURE 10. *(Continued.)* **Inversion results and corresponding errors for the inputted random wind fields: (a) Inversion result of the designed X-band multimode microwave remote sensor with low wind speed; (b) Inversion errors of the designed X-band multimode microwave remote sensor with low wind speed; (c) Inversion result of the HY-2 satellite with low wind speed; (d) Inversion error of the HY-2 satellite with low wind speed; (e) Inversion result of the QuikSCAT satellite with low wind speed; (f) Inversion error of the QuikSCAT satellite with low wind speed; (g) Inversion result of the designed X-band multimode microwave remote sensor with medium wind speed; (h) Inversion errors of the designed X-band multimode microwave remote sensor with medium wind speed; (i) Inversion result of the HY-2 satellite with medium wind speed; (j) Inversion error of the HY-2 satellite with medium wind speed; (k) Inversion result of the QuikSCAT satellite with medium wind speed; (l) Inversion error of the QuikSCAT satellite with medium wind speed; (m) Inversion result of the designed X-band multimode microwave remote sensor with high wind speed; (n) Inversion errors of the designed X-band multimode microwave remote sensor with high wind speed; (o) Inversion result of the HY-2 satellite with high wind speed; (p) Inversion error of the HY-2 satellite with high wind speed; (q) Inversion result of the QuikSCAT satellite with high wind speed; (r) Inversion error of the QuikSCAT satellite with high wind speed.**

IV. SIMULATION AND RESULTS

A. THE SETTING OF THE INPUTTED WIND FIELDS

For the sake of generality, this paper selects random and real wind fields as input wind fields. For these two types of wind fields, wind fields with low, medium and high wind speeds are set or selected. The random wind fields used in the simulation are set as a low-speed Gaussian wind field with a mean value of 5 m/s and a standard deviation of 2 m/s, a medium-speed Gaussian wind field with a mean value of 10 m/s and a standard deviation of 2 m/s, and a high-speed Gaussian wind

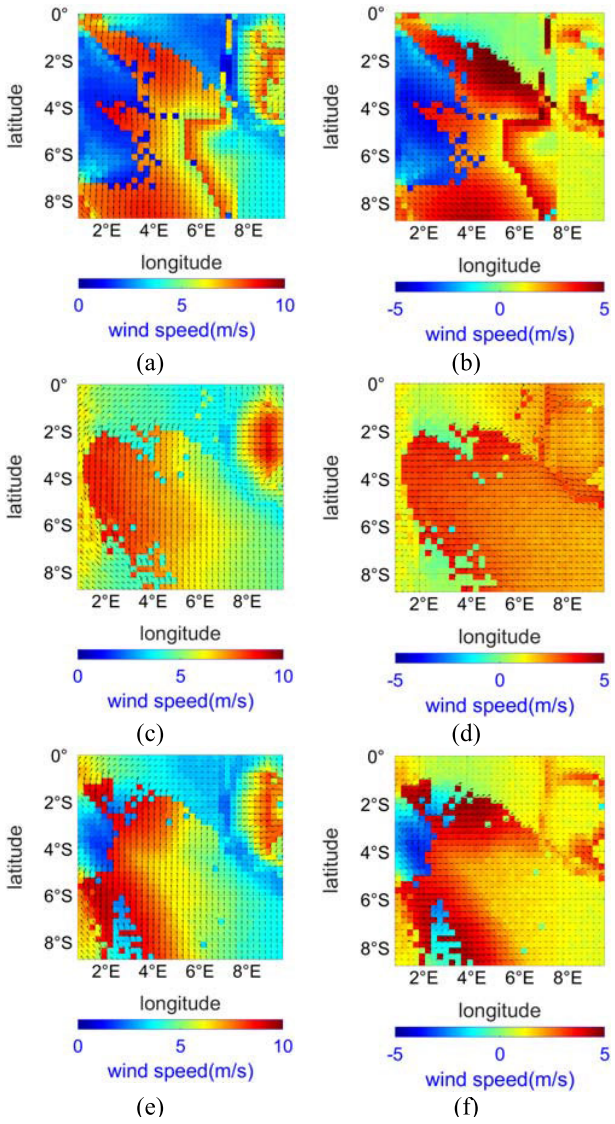

FIGURE 11. Inversion results and corresponding errors for the inputted real wind fields: (a) Inversion result of the designed X-band multimode microwave remote sensor with low wind speed; (b) Inversion errors of the designed X-band multimode microwave remote sensor with low wind speed; (c) Inversion result of the HY-2 satellite with low wind speed; (d) Inversion error of the HY-2 satellite with low wind speed; (e) Inversion result of the QuikSCAT satellite with low wind speed; (f) Inversion error of the QuikSCAT satellite with low wind speed; (g) Inversion result of the designed X-band multimode microwave remote sensor with medium wind speed; (h) Inversion errors of the designed X-band multimode microwave remote sensor with medium wind speed; (i) Inversion result of the HY-2 satellite with medium wind speed; (j) Inversion error of the HY-2 satellite with medium wind speed; (k) Inversion result of the QuikSCAT satellite with medium wind speed; (l) Inversion error of the QuikSCAT satellite with medium wind speed; (m) Inversion result of the designed X-band multimode microwave remote sensor with high wind speed; (n) Inversion errors of the designed X-band multimode microwave remote sensor with high wind speed; (o) Inversion result of the HY-2 satellite with high wind speed; (p) Inversion error of the HY-2 satellite with high wind speed; (q) Inversion result of the QuikSCAT satellite with high wind speed; (r) Inversion error of the QuikSCAT satellite with high wind speed.

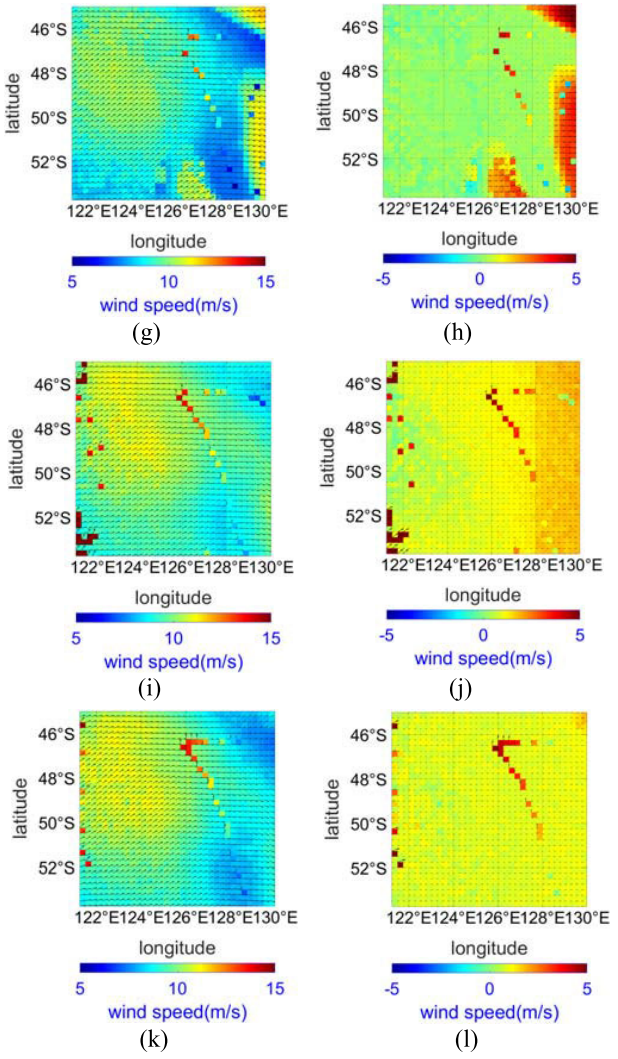

FIGURE 11. *(Continued.)* Inversion results and corresponding errors for the inputted real wind fields: (a) Inversion result of the designed X-band multimode microwave remote sensor with low wind speed; (b) Inversion errors of the designed X-band multimode microwave remote sensor with low wind speed; (c) Inversion result of the HY-2 satellite with low wind speed; (d) Inversion error of the HY-2 satellite with low wind speed; (e) Inversion result of the QuikSCAT satellite with low wind speed; (f) Inversion error of the QuikSCAT satellite with low wind speed; (g) Inversion result of the designed X-band multimode microwave remote sensor with medium wind speed; (h) Inversion errors of the designed X-band multimode microwave remote sensor with medium wind speed; (i) Inversion result of the HY-2 satellite with medium wind speed; (j) Inversion error of the HY-2 satellite with medium wind speed; (k) Inversion result of the QuikSCAT satellite with medium wind speed; (l) Inversion error of the QuikSCAT satellite with medium wind speed; (m) Inversion result of the designed X-band multimode microwave remote sensor with high wind speed; (n) Inversion errors of the designed X-band multimode microwave remote sensor with high wind speed; (o) Inversion result of the HY-2 satellite with high wind speed; (p) Inversion error of the HY-2 satellite with high wind speed; (q) Inversion result of the QuikSCAT satellite with high wind speed; (r) Inversion error of the QuikSCAT satellite with high wind speed.

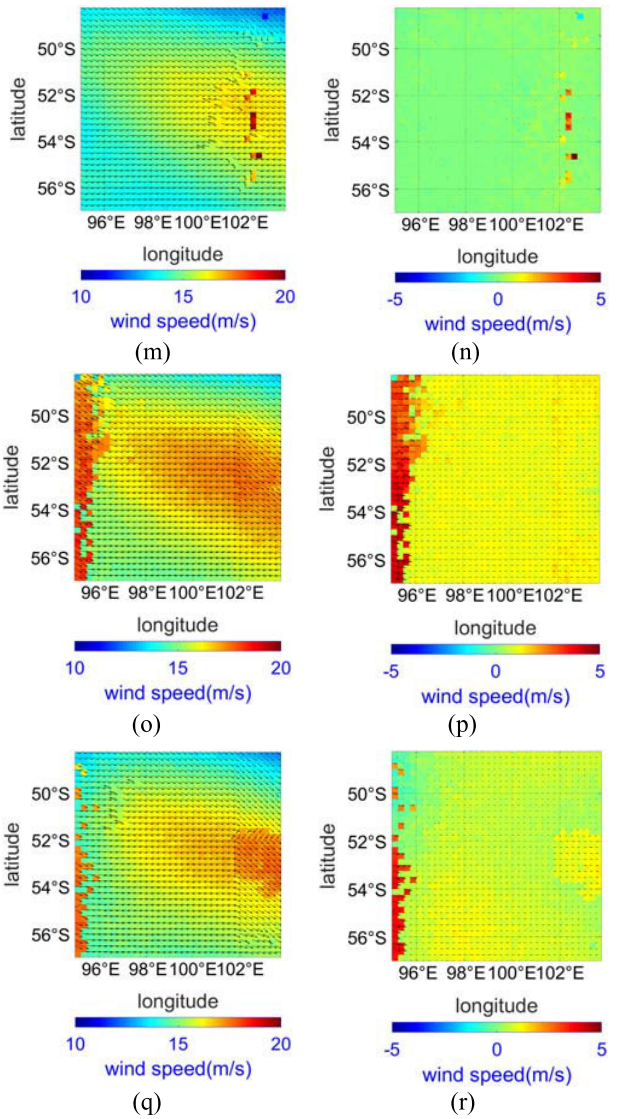

FIGURE 11. *(Continued.)* **Inversion results and corresponding errors for the inputted real wind fields: (a) Inversion result of the designed X-band multimode microwave remote sensor with low wind speed; (b) Inversion errors of the designed X-band multimode microwave remote sensor with low wind speed; (c) Inversion result of the HY-2 satellite with low wind speed; (d) Inversion error of the HY-2 satellite with low wind speed; (e) Inversion result of the QuikSCAT satellite with low wind speed; (f) Inversion error of the QuikSCAT satellite with low wind speed; (g) Inversion result of the designed X-band multimode microwave remote sensor with medium wind speed; (h) Inversion errors of the designed X-band multimode microwave remote sensor with medium wind speed; (i) Inversion result of the HY-2 satellite with medium wind speed; (j) Inversion error of the HY-2 satellite with medium wind speed; (k) Inversion result of the QuikSCAT satellite with medium wind speed; (l) Inversion error of the QuikSCAT satellite with medium wind speed; (m) Inversion result of the designed X-band multimode microwave remote sensor with high wind speed; (n) Inversion errors of the designed X-band multimode microwave remote sensor with high wind speed; (o) Inversion result of the HY-2 satellite with high wind speed; (p) Inversion error of the HY-2 satellite with high wind speed; (q) Inversion result of the QuikSCAT satellite with high wind speed; (r) Inversion error of the QuikSCAT satellite with high wind speed.**

field with a mean value of 15 m/s and a standard deviation of 2 m/s. It is noted that 50 simulations were performed in the setting of the random wind fields to reduce the uncertainties in the inverted results. Fig. 7 shows one of the distributions of the random wind fields under three wind speeds set in the simulation. Data downloaded from the European Centre for Medium-Range Weather Forecasts (ECMWF) website are used for the real wind field [35]–[37]. Public datasets of ECMWF Reanalysis-Interim (ERA-Interim) were accessed, and a datafile of .nc format was downloaded after choosing the year, month, time, 10 m U wind component, 10 m V wind component, longitude and latitude ranges, and grid size. We chose the grid size of $0.25° \times 0.25°$ to match the resolution level of 25 km. Global data were downloaded from the website to facilitate the selection of wind fields. After obtaining the datafile, the wind fields with low, medium, and high speeds were selected by manual analysis. Fig. 8 shows the real wind field distribution under three wind speeds in our experiment.

B. DATA PROCESSING FLOW

First, according to the requirements of the performance indicators, the system parameters of the multimode microwave remote sensor operating in scatterometer modes were designed. Then, the system simulation was carried out by using the designed system parameters, and the inversion errors under low, medium and high wind speeds were calculated. Afterwards, the system parameters of the scatterometers on the HY-2 satellite and on the QuikSCAT satellite were used to calculate the inversion accuracies for the same input wind fields. Finally, we compared the inversion errors of the multimode microwave remote sensor operating in the scatterometer mode, the inversion errors of scatterometers on the HY-2 satellite and on the QuikSCAT satellite in the simulation, and the typical values of inversion errors of scatterometers on the HY-2 satellite [38], [39] and on the QuikSCAT satellite [40], [41].

C. SYSTEM PARAMETER DESIGN RESULTS AND INVERSION ERRORS OF MULTIMODE MICROWAVE REMOTE SENSORS OPERATING IN SCATTEROMETER MODES

According to the requirements of the performance indicators and the set system parameters shown in Table 2, the system parameters of the multimode microwave remote sensor operating in the scatterometer mode were designed by using the method described in Section II. Table 3 shows the design results of the system parameters. For convenience of comparison, Table 4 and Table 5 present the corresponding parameters from the HY-2 system [15], [42] and the QuikSCAT system [17]. The signal bandwidth in Table 3 was calculated by the optimization method. Fig. 9 shows the variations in the RMS errors of wind speed and wind direction under different wind speed and bandwidth conditions for the selected real wind fields and verifies that the RMS errors of wind speed and wind direction corresponding to the outputted bandwidth value in Table 3, i.e., 1 MHz, are the minimum. It is necessary to point out that the essence of the performance comparison of different bandwidths is the performance comparison of different noise levels according to equation (26).

TABLE 2. Performance indicators and set system parameters used in designing the system parameters for the multimode microwave remote sensor operated in scatterometer mode.

range and azimuth resolution	25 km	backscattering coefficient accuracy	0.5 dB
internal beam swath	1400 km	external beam swath	1800 km
platform height	530 km	platform speed	7600 m/s
carrier frequency	9.6 GHz	system loss	7 dB
receiver noise figure	5 dB	pulse width	1.5 ms

TABLE 3. System parameter design results for the multimode microwave remote sensor operated in scatterometer mode.

internal beam's view angle	50.9°	internal beam's incidence angle	57.2°
external beam's view angle	56.5°	external beam's incidence angle	64.6°
antenna rotation speed	17 rpm	PRF minimum	127 Hz
PRF maximum	6106 Hz	PRF	191 Hz
azimuth antenna size	1.12 m	peak transmit power	75 W
range antenna size	2.08 m	signal bandwidth	1 MHz
bandwidth after dechirp	238 KHz	signal-to-noise ratio	10 dB

TABLE 4. System parameters of the scatterometer system mounted on HY-2 satellite.

range and azimuth resolution	25 km	backscattering coefficient accuracy	0.5 dB
internal beam swath	1400 km	external beam swath	1800 km
platform height	970 km	platform speed	7369 m/s
carrier frequency	13.25 GHz	pulse width	1.5 ms
internal beam's view angle	35°	internal beam's incidence angle	41.2°
external beam's view angle	40.5°	external beam's incidence angle	48.4°
antenna rotation speed	16.67 rpm	PRF	185 Hz
azimuth antenna size	1 m	peak transmit power	120 W
range antenna size	1 m	signal bandwidth	5 MHz
bandwidth after dechirp	640 kHz	signal-to-noise ratio	10 dB

TABLE 5. System parameters of the scatterometer system mounted on QuikSCAT satellite.

range and azimuth resolution	26 km	backscattering coefficient accuracy	0.5 dB
internal beam swath	1400 km	external beam swath	1800 km
platform height	803 km	platform speed	7454 m/s
carrier frequency	13.402 GHz	pulse width	1.5 ms
internal beam's view angle	40°	internal beam's incidence angle	46.4°
external beam's view angle	46°	external beam's incidence angle	54.1°
antenna rotation speed	18 rpm	PRF	185 Hz
azimuth antenna size	1 m	peak transmit power	110 W
range antenna size	1 m	signal bandwidth	375 kHz
bandwidth after dechirp	48 kHz	signal-to-noise ratio	10 dB

Using the set parameters in Table 2 and the system parameter design results shown in Table 3, the system simulation was carried out according to the method described in Section III. Fig. 10 and Fig. 11 show the inversion results of the inputted random and real wind fields, respectively. Table 6 lists the wind field inversion errors of the multimode microwave remote sensor operating in the scatterometer mode. The system simulation was also carried out according to the system simulation method described in Section III using the system parameters of the HY-2 satellite [15], [42] and the system parameters of the QuikSCAT satellite [17]. Fig. 10 and Fig. 11 also show the inversion results of the inputted random and real wind fields, respectively, for the simulation using the system parameters of the HY-2 satellite and the systems parameters of the QuikSCAT satellite. Table 7 and Table 8 list the wind field inversion errors corresponding to the simulation using the system parameters of the HY-2 satellite and the system parameters of the QuikSCAT satellite, respectively.

D. RESULT ANALYSIS

According to Table 6, Table 7 and Table 8, the inversion accuracies of wind speed and wind direction when using the designed system parameters of multimode microwave remote sensors operating in the scatterometer mode are similar to those of the results using the system parameters of the HY-2 satellite and the system parameters of the QuikSCAT satellite. According to [38]–[41], the typical RMS inversion errors of wind direction and wind speed measured by the HY-2 satellite and by the QuikSCAT satellite are approximately 25.3° and 1.44 m/s and approximately 20° and 1.85 m/s, respectively, which are roughly

TABLE 6. Wind field inversion errors of the designed multimode microwave remote sensor operated in scatterometer mode under different wind speeds.

test wind speed	RMS error of wind speed (m/s)	RMS error of wind direction (°)
random wind field with low speed	2.1	27.5
random wind field with medium speed	1.3	15.1
random wind field with high speed	0.6	16.8
real wind field with low speed	2.4	35.3
real wind field with medium speed	0.8	11.3
real wind field with high speed	0.7	21.3

TABLE 7. Wind field inversion errors of the simulation using system parameters of the HY-2 satellite under different wind speeds.

test wind speed	RMS error of wind speed (m/s)	RMS error of wind direction (°)
low-speed random wind field	1.9	23.4
medium-speed random wind field	1.5	12.9
high-speed random wind field	1.3	20.5
low-speed real wind field	2.2	32.3
medium-speed real wind field	1.4	14.2
high-speed real wind field	1.3	24.1

TABLE 8. Wind field inversion errors of the simulation using system parameters of the QuikSCAT satellite under different wind speeds.

test wind speed	RMS error of wind speed (m/s)	RMS error of wind direction (°)
low-speed random wind field	1.8	24.2
medium-speed random wind field	1.4	12.8
high-speed random wind field	1.0	19.3
low-speed real wind field	2.3	33.4
medium-speed real wind field	1.2	12.3
high-speed real wind field	1.0	22.1

equivalent to the errors of our simulation results. According to Table 2, Table 4 and Table 5, the resolution and swath of the designed multimode microwave remote sensor operating in the scatterometer mode are roughly the same as those of the HY-2 satellite [42] and the QuikSCAT satellite [17].

In summary, the designed multimode microwave remote sensor operating in the X-band at a height of 530 km can achieve roughly equivalent resolution, swath width and wind field inversion accuracy as specialized spaceborne scatterometers such as on the HY-2 satellite and on the QuikSCAT satellite. Additionally, the designed multimode microwave remote sensor combines the advantages of SAR, scatterometer, altimeter, and spectrometer and thus is very flexible given its ability to switch between several operation modes according to the user requirements. In other words, the designed multimode microwave remote sensor can realize both high-precision target detection and high-precision inversion of dynamic marine parameters. Certainly, it should be noted that the switching of the operation mode may affect the revisit time of the observation products to a certain extent. This can be overcome by networking two or more satellites to observe synchronously and allocate each satellite operating in a fixed mode. Moreover, a satellite operating in the spectrometer mode usually does not collect data when it passes through land areas, so at such time it can be switched to the SAR mode to improve the utilization of satellite resources. This kind of mode switch also does not affect the revisit time of the products of the spectrometer mode.

V. CONCLUSION

The multimode microwave remote sensor is a new radar system mounted on a small satellite platform. It combines the advantages of SAR, scatterometer, altimeter, and spectrometer instruments and is highly flexible. The SAR mode is the main mode of this new radar system. Some important parameters, such as the carrier frequency and the platform height of other modes, must be consistent with those of the SAR mode. Because the platform height, carrier frequency and other important parameters are different from the typical values of specialized spaceborne scatterometers, this paper studies the system parameter design method of the multimode microwave remote sensor system operating in scatterometer mode in order to provide the antenna rotation speed, effective antenna size, transmission power, pulse repetition frequency, signal bandwidth and other parameters. To verify the rationality of the parameter design results, the system simulation method of the scatterometer mode is also studied.

The results of the performed simulations show that, using the designed system parameters, the multimode microwave remote sensor system can obtain an inversion accuracy for the wind field comparable to those of the HY-2 satellite and the QuikSCAT satellite, and the corresponding resolution and swath width are almost equivalent to those of the HY-2 satellite and the QuikSCAT satellite. Furthermore, the designed multimode microwave remote sensor has high flexibility, so it has good development prospects.

ACKNOWLEDGMENT

The authors would like to thank the European Centre for Medium-Range Weather Forecasts (ECMWF) for the real wind field data.

They would also like to thank the anonymous reviewers for their valuable comments and suggestions, which helped substantially improve the quality of this paper.

REFERENCES

[1] W. Lv, P. Zhou, Y. Wang, X. Zhang, Y. Wan, and X. Qu, "Parameter design of multi—Mode small satellite SAR system," in *Proc. IEEE Int. Geosci. Remote Sens. Symp.*, Yokohama, Japan, Aug. 2019, pp. 8617–8620.

[2] P. Zhou, W. Lv, Z. Zhang, Y. Wang, X. Zhang, and Y. Dai, "System parameter design of multimodal small satellite SARs operating in scan mode and transmit power optimization for marine scenes," *IEEE Access*, vol. 8, pp. 36974–36987, Mar. 2020.

[3] S. Y. Kim, J. B. Sung, and A. Torre, "In-orbit antenna pattern extraction method for active phased-array SAR antennas," *IEEE Antennas Wireless Propag. Lett.*, vol. 15, pp. 317–320, Feb. 2016.

[4] M.-H. Ka and A. I. Baskakov, "Optimal discriminator and limiting accuracy of height measurement for a spaceborne oceanographic radar altimeter," *IEEE Geosci. Remote Sens. Lett.*, vol. 16, no. 3, pp. 332–336, Mar. 2019.

[5] R. Yun, X. Dong, L. Zhang, D. Zhu, Z. Wang, and J. Ma, "CFOSAT scatterometer data level-1 processing and preliminary results," in *Proc. IEEE Int. Geosci. Remote Sens. Symp. (IGARSS)*, Yokohama, Japan, Jul. 2019, pp. 8011–8014.

[6] W. Lin, X. Dong, M. Portabella, S. Lang, Y. He, R. Yun, Z. Wang, X. Xu, D. Zhu, and J. Liu, "A perspective on the performance of the CFOSAT rotating fan-beam scatterometer," *IEEE Trans. Geosci. Remote Sens.*, vol. 57, no. 2, pp. 627–639, Feb. 2019.

[7] A. Jordan, C. Purves, and J. Diggs, "An analysis of Skylab II S193 scatterometer data," *IEEE Trans. Geosci. Electron.*, vol. GE-14, no. 2, pp. 97–100, Apr. 1976.

[8] W. Grantham, E. Bracalente, W. Jones, and J. Johnson, "The SeaSat—A satellite scatterometer," *IEEE J. Ocean. Eng.*, vol. OE-2, no. 2, pp. 200–206, Apr. 1977.

[9] D. Schuler, "An experimental study of a pulse compression scatterometer system," *IEEE Trans. Antennas Propag.*, vol. AP-25, no. 1, pp. 140–145, Jan. 1977.

[10] E. P. W. Attema, "The active microwave instrument on-board the ERS-1 satellite," *Proc. IEEE*, vol. 79, no. 6, pp. 791–799, Jun. 1991.

[11] A. Bartoloni, C. D'Amelio, and F. Zirilli, "Wind reconstruction from Ku-band or C-band scatterometer data," *IEEE Trans. Geosci. Remote Sens.*, vol. 31, no. 5, pp. 1000–1008, Sep. 1993.

[12] D. Hauser, C. Tison, T. Amiot, L. Delaye, N. Corcoral, and P. Castillan, "SWIM: The first spaceborne wave scatterometer," *IEEE Trans. Geosci. Remote Sens.*, vol. 55, no. 5, pp. 3000–3014, May 2017.

[13] M. Lin, X. Ye, and X. Yuan, "The first quantitative joint observation of typhoon by Chinese GF-3 SAR and HY-2A microwave scatterometer," *Acta Oceanol. Sinica*, vol. 36, no. 11, pp. 1–3, Nov. 2017.

[14] A. S. Mironov, Y. Quilfen, and B. Chapron, "CFOSAT mission: Using of swim measurements for improving scat wind vector retrieval," in *Proc. IEEE Int. Geosci. Remote Sens. Symp. (IGARSS)*, Valencia, Spain, Jul. 2018, pp. 3258–3261.

[15] Y. Zhang, M. Lin, and Q. Song, "Evaluation of geolocation errors of the Chinese HY-2A satellite microwave scatterometer," *IEEE Trans. Geosci. Remote Sens.*, vol. 56, no. 10, pp. 6124–6133, Oct. 2018.

[16] J. Zhu, X. Dong, W. Lin, and X. Xu, "Calibration and estimation of attitude errors for a rotating fan-beam scatterometer using calibration ground stations," *IEEE J. Sel. Topics Appl. Earth Observ. Remote Sens.*, vol. 8, no. 1, pp. 171–179, Jan. 2015.

[17] J. E. Graf, W.-Y. Tsi, and L. Jones, "Overview of QuikSCAT mission—A quick deployment of a high resolution, wide swath scanning scatterometer for ocean wind measurement," in *Proc. IEEE Southeastcon Eng. New Era*, Orlando, FL, USA, Apr. 1998, pp. 314–317.

[18] J. Figa-Saldaña, J. J. W. Wilson, E. Attema, R. Gelsthorpe, M. R. Drinkwater, and A. Stoffelen, "The advanced scatterometer (ASCAT) on the meteorological operational (MetOp) platform: A follow on for European wind scatterometers," *Can. J. Remote Sens.*, vol. 28, no. 3, pp. 404–412, Jan. 2002.

[19] F. M. Naderi, M. H. Freilich, and D. G. Long, "Spaceborne radar measurement of wind velocity over the ocean—An overview of the NSCAT scatterometer system," *Proc. IEEE*, vol. 79, no. 6, pp. 850–866, Jun. 1991.

[20] P. K. Yoho and D. G. Long, "An improved simulation model for spaceborne scatterometer measurements," *IEEE Trans. Geosci. Remote Sens.*, vol. 41, no. 11, pp. 2692–2695, Nov. 2003.

[21] X. Dong, D. Zhu, W. Lin, H. Liu, and J. Jiang, "A Ku-band rotating fan-beam scatterometer: Design and performance simulations," in *Proc. IEEE Int. Geosci. Remote Sens. Symp.*, Honolulu, HI, USA, Jul. 2010, pp. 1081–1084.

[22] W. Lin, X. Dong, X.-O. Xu, D. Zhu, Z. Wang, and Y. He, "Performances of the rotating fanbeam scatterometer on CFOSAT," in *Proc. IEEE Int. Geosci. Remote Sens. Symp. (IGARSS)*, Valencia, Spain, Jul. 2018, pp. 1489–1492.

[23] M. W. Spencer, C. Wu, and D. G. Long, "Tradeoffs in the design of a spaceborne scanning pencil beam scatterometer: Application to SeaWinds," *IEEE Trans. Geosci. Remote Sens.*, vol. 35, no. 1, pp. 115–126, Jan. 1997.

[24] J. Zhu, X. Dong, W. Lin, and D. Zhu, "A preliminary study of the calibration for the rotating fan-beam scatterometer on CFOSAT," *IEEE J. Sel. Topics Appl. Earth Observ. Remote Sens.*, vol. 8, no. 2, pp. 460–470, Feb. 2015.

[25] C. Wang, J. Xu, G. Liao, X. Xu, and Y. Zhang, "A range ambiguity resolution approach for high-resolution and wide-swath SAR imaging using frequency diverse array," *IEEE J. Sel. Topics Signal Process.*, vol. 11, no. 2, pp. 336–346, Mar. 2017.

[26] A. Ribal and I. R. Young, "Global calibration and error estimation of altimeter, scatterometer, and radiometer wind speed using triple collocation," *Remote Sens.*, vol. 12, no. 2, pp. 1997–2016, May 2020.

[27] J. V. Toporkov and G. S. Brown, "Numerical simulations of scattering from time-varying, randomly rough surfaces," *IEEE Trans. Geosci. Remote Sens.*, vol. 38, no. 4, pp. 1616–1625, Jul. 2000.

[28] A. Stoffelen, J. A. Verspeek, J. Vogelzang, and A. Verhoef, "The CMOD7 geophysical model function for ASCAT and ERS wind retrievals," *IEEE J. Sel. Topics Appl. Earth Observ. Remote Sens.*, vol. 10, no. 5, pp. 2123–2134, May 2017.

[29] F. Nirchio and S. Venafra, "XMOD2—An improved geophysical model function to retrieve sea surface wind fields from cosmo-sky med X-band data," *Eur. J. Remote Sens.*, vol. 46, no. 1, pp. 583–595, Feb. 2017.

[30] J. Liu, Y. Zhang, and X. Dong, "Dechirping compression method for nonlinear frequency modulation waveforms," *IEEE Geosci. Remote Sens. Lett.*, vol. 16, no. 3, pp. 377–381, Mar. 2019.

[31] C. Zuo and H. Jiang, "A simulation method of target echo power," in *Proc. IEEE 4th Int. Conf. Signal Image Process. (ICSIP)*, Wuxi, China, Jul. 2019, pp. 294–298.

[32] Q. Feng, J. Zou, Q. Bao, and M. Lin, "Wind retrieval accuracy analysis of HY-2B microwave scatterometer," in *Proc. IEEE Int. Geosci. Remote Sens. Symp. (IGARSS)*, Yokohama, Japan, Jul. 2019, pp. 8023–8026.

[33] X. Xie, Z. Huang, M. Lin, K. Chen, Y. Lan, X. Yuan, X. Ye, and J. Zou, "A novel integrated algorithm for wind vector retrieval from conically scanning scatterometers," *Remote Sens.*, vol. 5, no. 12, pp. 6180–6197, Nov. 2013.

[34] D. X. Tian and X. T. Xie, "A study on polarimetric scatterometer simulation and wind vector," in *Proc. IEEE Int. Geosci. Remote Sens. Symp.*, Yokohama, Japan, Aug. 2019, pp. 8132–8135.

[35] European Centre for Medium-Range Weather Forecasts. *ECMWF | ERA Interim, Daily*. Accessed: Jul. 15, 2020. [Online]. Available: https://apps.ecmwf.int/datasets/data/interim-full-daily/levtype=sfc/

[36] S. Abdalla and G. De Chiara, "Estimating random errors of scatterometer, altimeter, and model wind speed data," *IEEE J. Sel. Topics Appl. Earth Observ. Remote Sens.*, vol. 10, no. 5, pp. 2406–2414, May 2017.

[37] X. T. Xie, J. Wang, and M. S. Lin, "A neural network-based rain effect correction method for HY-2A scatterometer backscatter measurements," *Remote Sens.*, vol. 10, no. 10, pp. 1648–1667, Apr. 2020.

[38] J. Yang and J. Zhang, "Accuracy assessment of HY-2A scatterometer wind measurements during 2011–2017 by comparison with buoys, ASCAT, and ERA-interim data," *IEEE Geosci. Remote Sens. Lett.*, vol. 16, no. 5, pp. 727–731, May 2019.

[39] K. Zhao and C. F. Zhao, "Evaluation of HY-2A scatterometer ocean surface wind data during 2012–2018," *Remote Sens.*, vol. 11, no. 24, pp. 2968–2990, Sep. 2019.

[40] R. T. Tonboe, "QuickScat-SeaWinds scatterometer observations of sea ice types around greenland," in *Proc. Remote Sens. Ocean Sea Ice*, Toulouse, France, Jan. 2002, pp. 46–58.

[41] N. Ebuchi, H. C. Graber, and M. J. Caruso, "Evaluation of ocean surface vector winds observed by QuikSCAT/SeaWinds and ADEOS-II/SeaWind," in *Proc. IEEE Int. Geosci. Remote Sens. Symp.*, Anchorage, AK, USA, Sep. 2004, pp. 795–798.
[42] X. Xu, X. Dong, D. Zhu, and S. Lang, "High winds from combined active and passive measurements of HY-2A satellite," *IEEE J. Sel. Topics Appl. Earth Observ. Remote Sens.*, vol. 11, no. 11, pp. 4339–4348, Nov. 2018.

PENG ZHOU (Member, IEEE) received the B.S. degree in electronic engineering and the M.S. degree in automation control engineering from the China University of Petroleum, Dongying, China, in 1997 and 2000, respectively, and the Ph.D. degree in signal and information processing from the University of Electronic Science and Technology of China, Chengdu, China, in 2008.

From December 2017 to November 2018, he worked as a Visiting Researcher with the Department of Information Engineering, University of Pisa, Italy. He is currently an Associate Professor with the College of Oceanography and Space Informatics, China University of Petroleum, Qingdao, China. His current research interests include SAR imaging, ISAR imaging, and remote sensing of oceans.

LIAN XUE received the B.S. degree in electronics and information engineering from the Shandong Youth University of Political Science, Jinan, China, in 2018. She is currently pursuing the M.S. degree with the College of Oceanography and Space Informatics, China University of Petroleum, Qingdao, China. Her research interests include parametric design of scatterometers, altimeters, and spectrometers and system simulation.

ZHENHUA ZHANG received the Ph.D. degree in signal processing from Xidian University, Xi'an, China, in 2007. He is currently a Researcher with the Beijing Research Institute of Telemetry, Beijing, China. His current research interests include SAR imaging and radar signal processing.

YING WANG received the M.S. degree in signal processing from Xidian University, Xi'an, China, in 2005. He is currently a Senior Engineer with the Beijing Research Institute of Telemetry, Beijing, China. His current research interests include radar signal processing and SAR systems.

XI ZHANG received the B.S. degree in information systems from the Qingdao University of Science and Technology, Qingdao, China, in 2005, and the M.S. degree in signal and information processing and the Ph.D. degree in computer science from the Ocean University of China, Qingdao, in 2008 and 2011, respectively.

He is currently an Associate Researcher with the First Institute of Oceanography, Ministry of Natural Resources of the People's Republic of China, Qingdao. His current research interests include remote sensing of oceans and SAR imaging.